nature communications

Article

https://doi.org/10.1038/s41467-025-57738-1

Topologically reconfigurable room-temperature polariton condensates from bound states in the continuum in organic metasurfaces

Received: 29 February 2024

Accepted: 3 March 2025

Published online: 10 March 2025

Check for updates

Xingchen Yan[1,2,5], Min Tang[3,5], Zhonghao Zhou[1], Libo Ma[3] ✉, Yana Vaynzof[3,4], Jiannian Yao[1,2], Haiyun Dong[1,2] ✉ & Yong Sheng Zhao[1,2] ✉

An exciton–polariton condensate is a state of matter with collective coherence leading to many fascinating macroscopic quantum effects. Recently, optical bound states in the continuum (BICs) have been demonstrated as peculiar topological states capable of imparting novel characteristics onto the polariton condensates. Organic semiconductors featuring robust Frenkel excitons and high physicochemical tunability potentially offer a promising platform to explore topologically engineering of BIC polariton condensates at room temperature. However, a universal physical mechanism for engineering organic BIC systems has remained elusive, hindering the demonstration of BIC polariton condensates with topologically tunable macroscopic quantum effects. Here we report topologically reconfigurable room-temperature polariton condensates by systematically engineering the BICs in organic semiconductor metasurfaces. Two-dimensional organic metasurfaces are designed to support two polariton BICs with different topological charges. The organic Frenkel excitons with large binding energies allow for non-equilibrium polariton condensation at BICs at room-temperature. By virtue of the excellent physicochemical tunability of organic materials, we further explore the dynamic topological engineering of polariton lasers by manipulating the BICs in situ. Our results fundamentally promote the innovative design and topological engineering of polaritonic materials and devices.

Exciton-polaritons are bosonic quasiparticles arising from strong coupling between semiconductor excitons and cavity photons, which can undergo condensation to macroscopically occupy the same quantum state[1–6]. Polariton condensates with collective coherence not only yield intriguing macroscopic quantum phenomena, including superfluidity and topological excitations[7–10], but also underpin functional polaritonic devices, such as ultralow-threshold lasers and ultrafast optical switches[11–15]. On the one hand, the polariton condensate leaks from the cavity as coherent light, constituting a captivating polariton laser[16,17]. On the other hand, the fast dissipation of exciton polaritons has been a major obstacle limiting the generation, propagation, and manipulation of polariton condensates[18–20].

[1]Key Laboratory of Photochemistry, Institute of Chemistry, Chinese Academy of Sciences, Beijing, China. [2]School of Chemical Science, University of Chinese Academy of Sciences, Beijing, China. [3]Leibniz Institute for Solid State and Materials Research Dresden, Dresden, Germany. [4]Chair for Emerging Electronic Technologies, Technische Universität Dresden, Dresden, Germany. [5]These authors contributed equally: Xingchen Yan, Min Tang.
✉e-mail: l.ma@ifw-dresden.de; donghaiyun@iccas.ac.cn; yszhao@iccas.ac.cn

Optical bound states in the continuum (BICs) with a non-radiative nature provide a platform to suppress the dissipation of exciton polaritons towards efficient polariton condensation[21,22]. Although first proposed in quantum mechanics, the BICs are a general wave phenomenon describing counterintuitive perfect wave confinement within the radiation continuum[23]. In optics, the BICs have been demonstrated as peculiar topological states with zero radiation in metasurfaces. The non-radiative BICs have infinitely high quality (Q) factors[24–29], which facilitate the formation of polaritons with sufficiently long lifetimes for polariton condensation[21,22]. More importantly, the topological nature of BICs can endow polariton condensates with fascinating characteristics, for example, symmetry protection and polarization vortex[30–37]. In particular, the polarization vortices carrying topological charges provide a new degree of freedom for polariton physics and applications.

So far, polariton condensation at BICs has been mainly explored in inorganic semiconductors, of which the Wannier-Mott excitons with small binding energies restrict the BIC polariton condensates to cryogenic temperature[21,22,38]. A particularly serious problem is that the topological properties of polariton condensates are fixed by the BIC metasurface geometries because the inorganic semiconductors generally lack in-situ tunability, making it fundamentally challenging to explore the dynamic topological engineering of BIC polariton condensates. By contrast, organic semiconductors feature large exciton binding energies[39–43], which has enabled room-temperature polariton condensations at BICs[44,45]. In particular, organic materials possess high physicochemical tunability[46–52], offering a promising platform for the design and control of BIC metasurface systems toward topologically variable BIC polariton condensates at room temperature.

In this work, we demonstrate the systematic engineering of BICs in organic metasurfaces, which enables topologically reconfigurable room-temperature polariton condensates. Two-dimensional metasurfaces of an organic semiconductor were designed to support two polariton BICs carrying different topological charges. Within the organic metasurfaces, the strong coupling between robust Frenkel excitons and infinitely high-Q BICs enabled room-temperature, non-equilibrium polariton condensation at BICs under ultralow thresholds. Furthermore, we explored the topological tuning of polariton lasers by engineering the BICs. The polariton lasing was successfully switched between two topologically distinct BICs by tailoring the structure parameters and, thus, the photonic band structures of organic metasurfaces. On this basis, we proposed an in-situ molecular photoisomerization strategy to engineer the organic metasurfaces in real time, which leads to dynamic tuning of topological charges of the BIC polariton laser. These results pave the way to achieving room-temperature BIC polariton condensates with topologically tunable macroscopic quantum effects.

Results and discussion

Strong coupling of Frenkel excitons with photonic BICs in an organic metasurface

Figure 1a schematically shows the polariton BIC device comprising a two-dimensional metasurface of an organic semiconductor sandwiched between two polymer layers. The organic metasurface was prepared by a standard lithographic method (Supplementary Figs. 1–3). A transparent poly(methyl methacrylate) (PMMA) film is patterned with a square array of circular holes to define the metasurface geometry. Next, a film of 2,7-bis(4-(9H-carbazol-9-yl)phenyl)-9,9′-

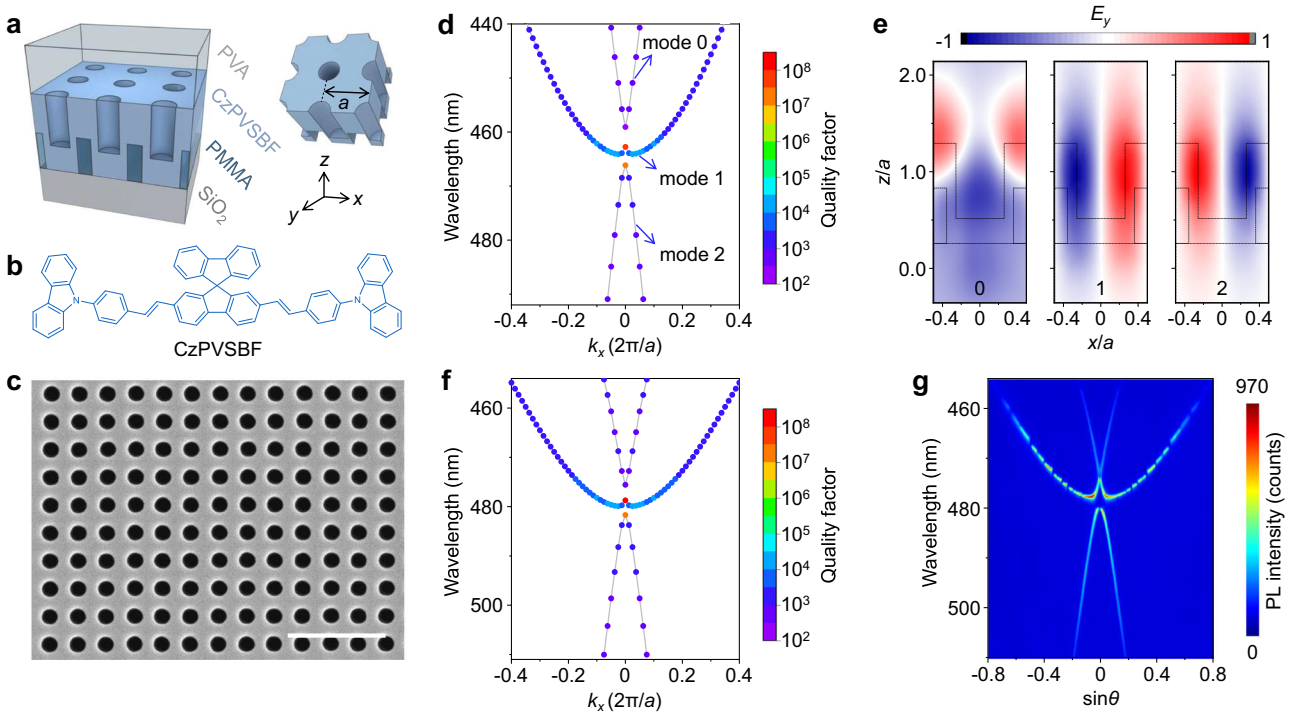

Fig. 1 | Strong coupling of Frenkel excitons with photonic BICs in an organic metasurface. a Schematic illustration of the polariton BIC device comprising a two-dimensional metasurface of an organic semiconductor film sandwiched between two polymer layers. PVA poly(vinyl alcohol), CzPVSBF 2,7-bis(4-(9H-carbazol-9-yl) phenyl)−9,9′-spirobifluorene, PMMA poly(methyl methacrylate), a is the period of the metasurface, and x, y, z are the wave-vector directions. **b** Molecular structure of CzPVSBF. **c** SEM image of a CzPVSBF film deposited on a PMMA pattern. Scale bar, 1 μm. **d** Calculated TE resonant modes around the CzPVSBF exciton emission and their quality factors from the finite element method. **e** Calculated electric field profiles for the E_y component of the photonic modes. The dashed lines outline the structural details in one unit cell of the metasurface. The modes 1 and 2 at the Γ point with ultrahigh Q factors and odd symmetries are two symmetry-protected BICs. **f** Calculated polariton dispersion based on strong coupling of the calculated photonic modes (**d**) with the excitonic resonance of CzPVSBF. **g** Polariton emission spectrum from a typical organic metasurface under non-resonant continuous-wave excitation. The two dark states at the Γ point ($\theta = 0$) correspond to two polariton BICs with non-radiative nature.

spirobifluorene (CzPVSBF, Fig. 1b) is deposited onto the PMMA pattern. The CzPVSBF molecule features a large exciton oscillator strength and a sufficient overlap between the exciton absorption and emission (Supplementary Figs. 4–6), which facilitates the reversible coherent exchange of energy between Frenkel excitons and cavity photons to form stable exciton polaritons at room temperature. Finally, a layer of poly(vinyl alcohol) (PVA) is spin-coated to protect the organic semiconductor film. Figure 1c displays a scanning electron microscope (SEM) image of a typical organic semiconductor metasurface with a period of $a = 280$ nm, a radius of $r = 80$ nm, and a hole depth of $h = 270$ nm (Supplementary Fig. 3). The fabricated organic metasurfaces have well-controlled structures (Supplementary Fig. 7), which is beneficial for exploring BICs with tailorable topological properties.

Optical resonances in the square organic metasurface were determined using the finite element method (Supplementary Fig. 8). Figure 1d shows three transverse electric (TE) resonant modes around the CzPVSBF exciton emission and their quality (Q) factors. Mode 0 is lossy with a low Q factor, while modes 1 and 2 have infinitely high Q factors at the high symmetry (Γ) point ($k_x = 0$). Figure 1e and Supplementary Fig. 9 show the calculated electric field profiles of the three modes at the Γ point. Mode 0 has electric field profiles with the same even symmetry as the free-space modes. Hence, the mode 0 leaks into free space, leading to finite Q factors. By contrast, modes 1 and 2 have electric field profiles with odd symmetries. The symmetry mismatch decouples modes 1 and 2 from the free-space modes, giving rise to two symmetry-protected BICs with infinite Q factors[21,23]. Henceforth, the modes 1 and 2 at the Γ point are referred to as BIC_1 and BIC_2, respectively.

Strong coupling between the organic Frenkel excitons and the photonic modes was theoretically investigated by a coupled oscillator model (Supplementary Note 1). Figure 1f exhibits the calculated exciton-polariton dispersion in the organic metasurface. Unlike the pure photonic modes 0 and 2 with almost constant curvatures, the polariton dispersion curvatures become smaller at short wavelengths and large angles, which is a typical result of strong coupling[14,53–55]. Figure 1g presents the angle-resolved microphotoluminescence (AR μ-PL) spectrum from a typical organic metasurface under non-resonant continuous-wave excitation at room temperature (Supplementary Fig. 10). Notate that there are many breakpoints in polariton dispersion curves away from the Γ point, which are induced by the weak radial modes confined in the PMMA layer (Supplementary Fig. 11)[56]. The experimentally measured dispersions of modes 0, 1, and 2 are in good agreement with the theoretically calculated polariton dispersions, indicating the occurrence of strong exciton-photon coupling in the organic metasurface. The strong coupling regime is also evidenced by a distinct anticrossing behavior of the lower and upper polariton branches in the reflectance spectra (Supplementary Fig. 12) and a bending effect of lower polariton branches in the PL spectra (Supplementary Figs. 13 and 14)[54,57]. The dispersions of polariton modes 1 and 2 reveal two dark states at the Γ point corresponding to two polariton BICs with non-radiative nature[21]. The Q factors of the polariton mode 2 exhibit a sudden divergence at the Γ point (Supplementary Fig. 15), confirming the formation of polariton BIC_2[36]. Such polariton BICs featuring ultrahigh Q factors would contribute to the realization of low-threshold polariton lasing.

Room-temperature polariton lasing at BICs in an organic metasurface

The organic metasurface was investigated under non-resonant pulsed excitation. At a low pump fluence ($P = 0.23$ μJ cm^{-2}), the polariton emission is distributed broadly along the whole dispersion curves of polariton modes 0, 1, and 2 (Fig. 2a). Upon increasing the pump fluence to 0.30 μJ cm^{-2}, two bright emission lobes appear near $\theta = 0$ for mode 2, corresponding to the polariton BIC_2 (Fig. 2b)[22]. When the pump

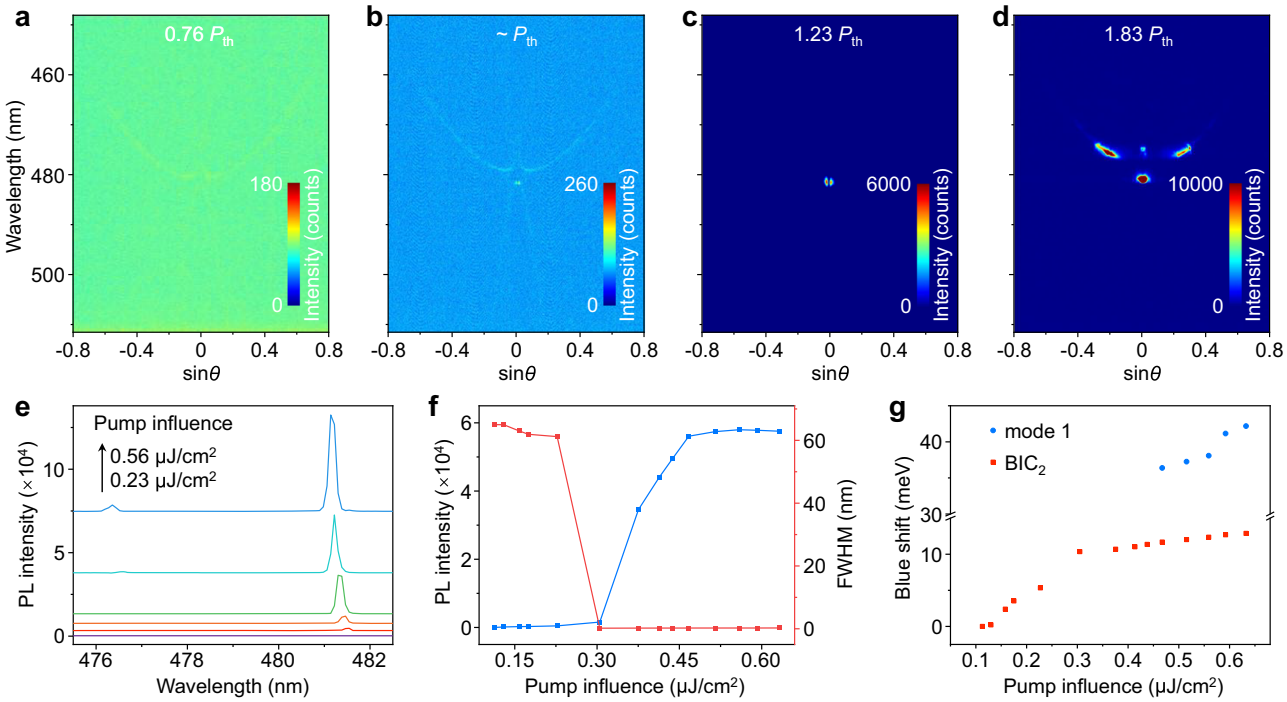

Fig. 2 | Polariton condensation at BICs in an organic metasurface. a–d Angle-resolved photoluminescence spectra from an organic metasurface under non-resonant pulsed excitations with different energy densities, 0.23 μJ cm^{-2} (**a**), 0.30 μJ cm^{-2} (**b**), 0.38 μJ cm^{-2} (**c**), and 0.56 μJ cm^{-2} (**d**). **a–c** show the polariton condensation at BIC_2, while **d** exhibits the scattering of polariton condensates from the BIC_2 to mode 1. The two bright emission lobes around the Γ point ($\theta = 0$) (**b**, **c**) are a typical characteristic of polariton BICs. **e** Evolution of the photoluminescence (PL) spectrum from the broad band to sharp peak with the pump fluence, revealing a polariton condensation threshold of 0.30 μJ cm^{-2} and an increase in temporal coherence of polariton emission. **f** Polariton emission intensities (blue) and full widths at half maximum (FWHMs) (red) near $\theta = 0$ versus the pump fluences. **g** Energy blueshift with respect to the BIC polariton emission energy as a function of the pump fluence, which is a typical result of polariton–exciton/polariton interactions.

https://doi.org/10.1038/s41467-025-57738-1

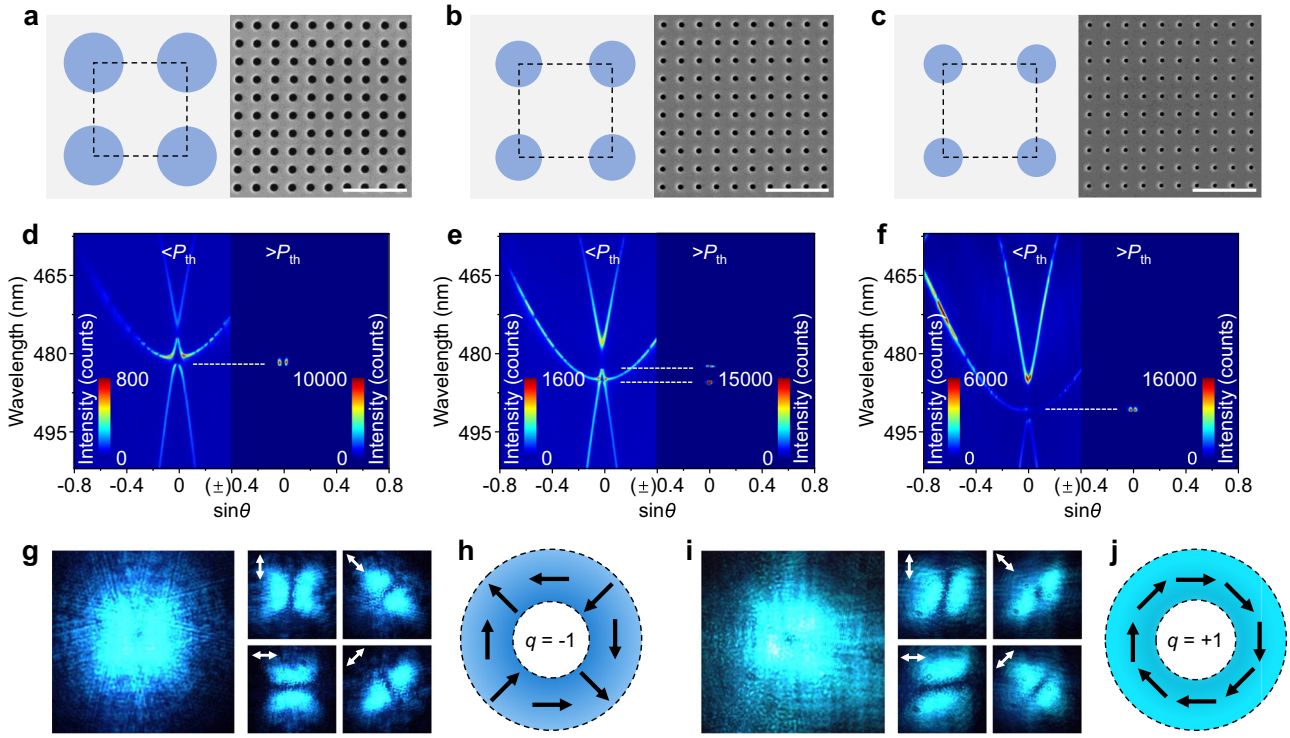

Fig. 3 | Topologically reconfigurable BIC polariton condensates in organic metasurfaces with tailorable structural parameters. a–c Schematic diagrams and SEM images of the organic metasurfaces with filling factors of 67.5% (**a**), 80.4% (**b**), and 85.6% (**c**). Scale bars, 1 μm. Angle-resolved photoluminescence spectra of the metasurfaces with filling factors of 67.5% (**d**), 80.4% (**e**), and 85.6% (**f**) below (left) and above (right) the polariton condensation threshold, showing the switching of polariton condensates from BIC_2 to BIC_1. Far-field patterns of BIC_2 (**g**) and BIC_1 (**i**) polariton condensates before and after passing through a linear polarizer with different polarization orientations. White arrows denote the directions of the linear polarizer along 0°, 45°, 90°, and 135°. Deduced polarization vector fields of the BIC_2 (**h**) and BIC_1 (**j**) polariton condensates. Black arrows indicate the polarization vector directions. The topological charges (q) carried by the BIC_2 and BIC_1 polariton condensates are −1 and +1, respectively.

fluence rises to 0.38 μJ cm^{-2}, the polariton BIC_2 dominates the emission of the organic metasurface (Fig. 2c). The dramatic emission enhancement and notable spectral narrowing in both energy and momentum suggest the occurrence of non-equilibrium polariton condensation at the polariton BIC_2[21]. Long-range spatial and temporal coherence verifies the formation of polariton condensates in the CzPVSBF metasurface (Supplementary Figs. 16 and 17)[21]. With a further increase of the pump fluence, the polariton condensates are scattered from BIC_2 to the polariton mode 1 including the BIC_1 (Fig. 2d). This result not only evidences the polariton–exciton/polariton repulsive interactions but also inspires the exploration of reconfigurable BIC polariton lasers.

The spectral characteristics were further analyzed to fully demonstrate the polariton lasing at BICs. Figure 2e shows the evolution of the polariton emission spectra from weak and broad to strong and sharp emissions with increasing pump fluences. The nonlinear increase in polariton emission intensity reveals a polariton lasing threshold of P_{th} = 0.30 μJ cm^{-2} (Fig. 2f), which is one to three orders of magnitude lower than those reported in traditional organic cavities based on distributed Bragg reflectors (Supplementary Table 1)[39,40,42,58]. In addition, the polariton condensation threshold in our organic semiconductor BIC metasurface is 1 order of magnitude lower than that of a dye-doped polymer on a silicon BIC metasurface[44,45] because the net organic semiconductor film has a higher molecular concentration than that of the dye-doped polymer film, which is beneficial for obtaining a larger exciton polariton density for lower-threshold polariton condensation. The extremely low polariton lasing threshold is attributed to the ultrahigh Q factors of polariton BICs. Beyond the threshold, the full width at half maximum (FWHM) of polariton emission collapses, indicating a notable increase in temporal coherence. Furthermore, the polariton emission exhibits a remarkable continuous blueshift upon increasing pump fluences due to the existence of polariton-exciton/polariton interactions (Fig. 2g)[4,39,59,60]. The strong polariton-exciton/polariton interactions scatter the polariton condensates from BIC_2 to the polariton mode 1 including BIC_1 (Fig. 2d, e, g). The large nonlinearity inherited from the exciton component of polaritons confirms that the strong and sharp emission originates from the polariton lasing rather than conventional photon lasing in the weak coupling regime[40].

Topological engineering of BIC polariton lasers

As shown in the calculated electric field profiles and polarization vector fields (Supplementary Figs. 18 and 19), the two BICs in the square metasurface carry different topological charges, showing great potential for exploring polariton lasers with different topological properties. Here, we propose a strategy of designing and tuning the band structures of the metasurfaces to achieve switchable polariton lasing between two BICs. The metasurface is characterized by a filling factor, which influences the energy gaps between different modes (Fig. 3a–f and Supplementary Fig. 20)[61,62]. As shown in Fig. 3a, d, a small energy gap between the polariton BIC_1 and mode 0 is observed in a metasurface with a small filling factor. Because of energy leakage from the BIC_1 to the lossy mode 0[22], polariton lasing occurs only at the BIC_2 (Fig. 3d) despite the fact that the BIC_1 has an intrinsically higher Q factor (Fig. 1d). With the increase of filling factor, the energy gap between the polariton BIC_1 and mode 0 increases gradually (Fig. 3a–f). Thus, polariton lasing begins to occur at the BIC_1 due to the reduction of energy leakage from this BIC. At a medium energy gap, two polariton lasing actions are observed at the BIC_1 and BIC_2 simultaneously (Fig. 3b, e). At a large energy gap, the polariton laser emission at BIC_1 dominates over that at BIC_2 (Fig. 3c, f). The polariton lasing threshold at BIC_1 is as low as 0.19 μJ cm^{-2} (Supplementary Fig. 21), owing to the

https://doi.org/10.1038/s41467-025-57738-1

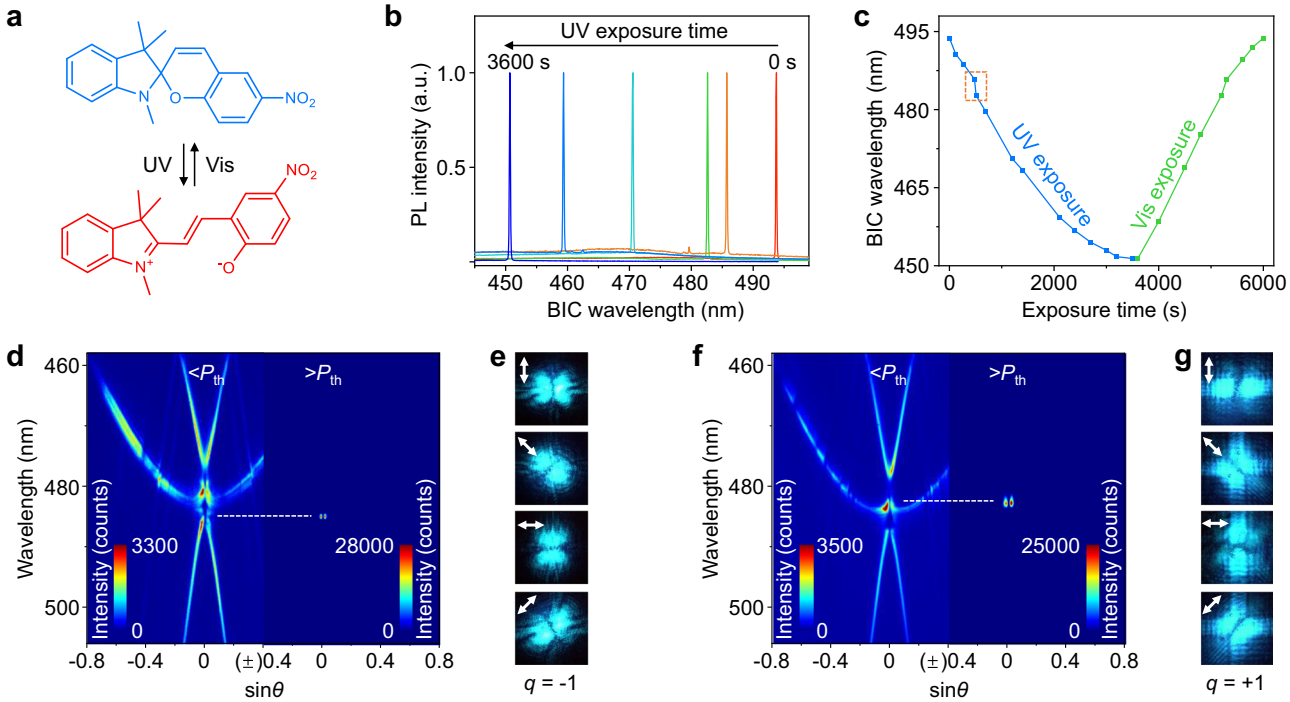

Fig. 4 | Dynamically tunable BIC polariton condensates based on in-situ molecular photoisomerization in an organic metasurface. a Reversible molecular photoisomerization of 1′,3′-dihydro-1′,3′,3′-trimethyl−6-nitrospiro[2H−1-benzopyran-2,2′-(2H)-indole] between spiropyran and merocyanine. As the spiropyran and merocyanine isomers have different refractive indices, this molecule is incorporated into the PMMA layer to tune the organic metasurface in real time. **b** Polariton lasing spectra of a typical organic semiconductor metasurface incorporated with the spiropyran upon UV exposure. **c** Plots of the polariton BIC laser wavelengths versus UV and Vis exposure times. The sudden decrease in wavelength from 486 to 483 nm (dash box) under UV exposure indicates a phase change of the BIC polariton condensates. **d**, **f** Angle-resolved photoluminescence spectra below (left) and above (right) polariton condensation thresholds before (**d**) and after (**f**) the phase change, showing a dynamic switching of polariton condensates from BIC_2 to BIC_1. **e**, **g** Far-field patterns of polariton condensates at 486 nm (**e**) and 483 nm (**g**) after passing through a linear polarizer with different polarization orientations. White arrows denote the directions of the linear polarizer along 0°, 45°, 90°, and 135°. The topological charges (q) carried by the polariton condensates at 486 nm and 483 nm are −1 and +1, respectively.

high Q factor of polariton BIC_1. The influences of different optical gain and polariton relaxation mechanisms on BIC polariton lasing positions are precluded (Supplementary Figs. 22 and 23), confirming that the energy gap-dependent energy leakage is the decisive factor driving the switching of polariton lasing between two BICs. The fitting of polariton distribution along mode 1 reveals the non-equilibrium nature of the polariton condensates (Supplementary Fig. 24)[17]. The controllable polariton lasing at different BICs allows for the investigation of polariton condensates with different topological properties.

The topological characteristics of the two BIC polariton condensates were investigated by probing the far-field intensity distributions of polariton lasers (Fig. 3g–i)[37]. Both BIC polariton condensates exhibit doughnut-shaped laser emission profiles in the far field, of which the dark centers are topological phase singularity points[63]. Upon passing through a linear polarizer, the laser emission profiles evolve from the doughnut shape into double-lobe shapes, and these lobes rotate with the polarizer, which reveals the polarization vortex nature of the BIC polariton lasers[64]. More interestingly, there is a notable difference in the lobe rotations, implying different topological properties. The BIC_1 and BIC_2 vortex laser lobes rotate in the same and opposite directions with respect to the polarizer, respectively, while at the same rate as that of the polarizer. This indicates that BIC_1 and BIC_2 polariton condensates carry topological charges of +1 and −1, respectively[65]. The polarization-dependent laser beam profiles further reveal the polarization vector fields of polariton condensates (Fig. 3h–j), which is in excellent agreement with the calculated polarization vortices with different topological charges (Supplementary Fig. 19). Taken together, we realized the imprinting of tunable topological charges to polariton lasers by exploiting tailorable BICs.

Organic materials feature high compatibility and flexibility, offering a possibility to further explore dynamically reconfigurable BIC polariton lasers. Here, we introduce an in-situ molecular photoisomerization strategy to tune the BIC polariton condensates in real time. A typical photoisomerizable spiropyran derivative, 1′,3′-dihydro-1′,3′,3′-trimethyl-6-nitrospiro[2H-1-benzopyran-2,2′-(2H)-indole] (Fig. 4a), is introduced into the PMMA layer. The BIPS doped PMMA pattern exhibits a well-defined, regular square array of circular holes (Supplementary Fig. 26), ensuring the following fabrication of the high-quality organic semiconductor metasurface. Upon UV light irradiation, the spiropyran molecule transforms into a merocyanine derivative with a higher refractive index, which can be reversed upon exposure to visible (Vis) light. Therefore, the molecular photoisomerization changes the refractive index contrast and optical resonances in the organic metasurface (Supplementary Figs. 27 and 28). Indeed, as shown in Fig. 4b, c the BIC polariton laser wavelength gradually shifts from 493 to 450 nm upon continuous UV exposure, which returns to its initial value once exposed to Vis light.

Besides the real-time tunable laser wavelengths, the molecular photoisomerization promises to endow the polariton lasers with dynamically switchable topological charges. The photoisomerization-induced change in the refractive index contrast would alter the band structure of the metasurface[66,67] towards topologically reconfigurable polariton lasers. As shown in Fig. 4c, the laser wavelength undergoes a sudden decrease from 486 to 483 nm upon UV exposure, suggesting a phase change of polariton condensates between the two different BICs. Measured dispersion curves demonstrate that the polaritons initially condensate at the lower BIC_2 (≥486 nm) and then switch to the upper BIC_1 (≤483 nm) (Fig. 4d, f). The dynamic switching of polariton

lasing from BIC_2 to BIC_1 is attributed to the expanded energy gap that reduces the energy leakage from the BIC_1 to the lossy mode 0. Far-field laser beam profiles further confirm the polarization vortex nature and different topological charges of the two kinds of BIC polariton condensates (Fig. 4e–g and Supplementary Fig. 29). The polariton lasers exhibit excellent reversibility and repeatability in both wavelengths and topological charges (Supplementary Fig. 30). Overall, we realized in-situ dynamic topological engineering of polariton lasers by manipulating the BICs in a reconfigurable manner.

In summary, we established that organic metasurfaces make it possible to realize ultralow-threshold room-temperature non-equilibrium polariton condensation at BICs and control the topological properties of BIC polariton condensates. We synthesized all-organic metasurfaces supporting ultralow-threshold polariton lasing at room temperature by integrating the advantages of organic Frenkel excitons and photonic BICs. Furthermore, both static and dynamic topological reconfiguring of BIC polariton lasers were realized by tailoring the band structures of the organic metasurfaces with materials engineering strategies. The high Q factors and long lifetimes of BICs provide a possibility for exploring quasi-equilibrium polariton condensation by suppressing the dissipation of exciton polaritons. This work offers striking advances in the application of organic material systems as a diverse platform for exploring novel photonic and polaritonic BICs.

Methods

Materials

Poly(methyl methacrylate) (PMMA, M.W. 350,000) and poly(vinyl alcohol) (PVA, M.W. 20000) were purchased from Sigma-Aldrich. 2,7-bis(4-(9H-carbazol-9-yl)phenyl)-9,9′-spirobifluorene (CzPVSBF) was purchased from Shanghai Daran Chemical Co., Ltd. 1′,3′-dihydro-1′,3′,3′-trimethyl-6-nitrospiro[2H-1-benzopyran-2,2′-(2H)-indole] (BIPS) was purchased from TCI (Shanghai). Organic solvents, including isopropanol (IPA, 99.9%), methyl isobutyl ketone (MIBK, 99.9%), acetone (99.9%), and chlorobenzene (99.9%), were acquired from Beijing Chemical Reagent Co., Ltd. All these materials were used as received without further treatment.

Sample fabrication

The organic metasurfaces were prepared by a standard lithographic method (Supplementary Fig. 1).

Morphology and structural characterizations

The morphology of the metasurface was characterized by a scanning electron microscope (SEM, FEI Nova NanoSEM 450) and an atomic force microscope (AFM, Bruker Multimode 8).

Optical characterization

Absorption spectra and fluorescence spectra were measured on a UV–visible spectrophotometer (Hitachi UH4150) and a fluorescence spectrometer (Hitachi F-7000), respectively. Fluorescence microscopy images were taken using an inverted fluorescence microscope (Nikon Ti-U) with a mercury lamp (Nikon). Refractive indices were measured on a spectroscopic ellipsometer (Sentech SE850 DUV). A portable UV (365 nm) lamp was used to induce molecular photoisomerization. Angle-resolved photoluminescence spectra (AR μ-PL) were measured based on Fourier optics (Supplementary Fig. 8). Spatial and temporal coherence were characterized by a Michelson interferometer.

Numerical simulations

Photonic band structures, electric field profiles, quality factors, and polarization vector distributions of the organic metasurface were calculated with a finite-element method using COMSOL Multiphysics (Supplementary Fig. 7). Polariton dispersion curves were calculated through the coupled oscillator model (Supplementary Note 1).

Data availability

The authors declare that all data to evaluate the conclusions are available within the article and its Supplementary Information files. Source data are provided with this paper.

Code availability

The codes used in this work are available from the corresponding authors upon request.

References

1. Deng, H. et al. Condensation of semiconductor microcavity exciton polaritons. *Science* **298**, 199–202 (2002).
2. Kéna-Cohen, S. & Forrest, S. Room-temperature polariton lasing in an organic single-crystal microcavity. *Nat. Photonics* **4**, 371–375 (2010).
3. Georgiou, K. et al. Ultralong-range polariton-assisted energy transfer in organic microcavities. *Angew. Chem. Int. Ed.* **133**, 16797–16803 (2021).
4. Su, R. et al. Perovskite semiconductors for room-temperature exciton-polaritonics. *Nat. Mater.* **20**, 1315–1324 (2021).
5. Jiang, Z. et al. Exciton-polaritons and their Bose-Einstein condensates in organic semiconductor microcavities. *Adv. Mater.* **34**, 2106095 (2022).
6. Hirai, K., Hutchison, J. A. & Uji-i, H. Molecular chemistry in cavity strong coupling. *Chem. Rev.* **123**, 8099–8126 (2023).
7. Lerario, G. et al. Room-temperature superfluidity in a polariton condensate. *Nat. Phys.* **13**, 837–841 (2017).
8. Klembt, S. et al. Exciton-polariton topological insulator. *Nature* **562**, 552–556 (2018).
9. Lagoudakis, K. et al. Observation of half-quantum vortices in an exciton-polariton condensate. *Science* **326**, 974–976 (2009).
10. Amo, A. et al. Polariton superfluids reveal quantum hydrodynamic solitons. *Science* **332**, 1167–1170 (2011).
11. Sanvitto, D. & Kéna-Cohen, S. The road towards polaritonic devices. *Nat. Mater.* **15**, 1061–1073 (2016).
12. St-Jean, P. et al. Lasing in topological edge states of a one-dimensional lattice. *Nat. Photonics* **11**, 651–656 (2017).
13. Feng, J. et al. All-optical switching based on interacting exciton polaritons in self-assembled perovskite microwires. *Sci. Adv.* **7**, eabj6627 (2021).
14. De, J. et al. Room-temperature electrical field-enhanced ultrafast switch in organic microcavity polariton condensates. *J. Am. Chem. Soc.* **145**, 1557–1563 (2023).
15. Castellanos, G. W. et al. Non-equilibrium Bose–Einstein condensation of exciton–polaritons in silicon metasurfaces. *Adv. Opt. Mater.* **11**, 2202305 (2023).
16. Bloch, J., Carusotto, I. & Wouters, M. Non-equilibrium Bose–Einstein condensation in photonic systems. *Nat. Rev. Phys.* **4**, 470–488 (2022).
17. Byrnes, T., Kim, N. Y. & Yamamoto, Y. Exciton–polariton condensates. *Nat. Phys.* **10**, 803–813 (2014).
18. Sun, Y. et al. Bose-Einstein condensation of long-lifetime polaritons in thermal equilibrium. *Phys. Rev. Lett.* **118**, 016602 (2017).
19. Wertz, E. et al. Spontaneous formation and optical manipulation of extended polariton condensates. *Nat. Phys.* **6**, 860–864 (2010).
20. Li, Y. et al. Manipulating polariton condensates by Rashba-Dresselhaus coupling at room temperature. *Nat. Commun.* **13**, 3785 (2022).
21. Ardizzone, V. et al. Polariton Bose–Einstein condensate from a bound state in the continuum. *Nature* **605**, 447–452 (2022).
22. Riminucci, F. et al. Nanostructured Ga As/(Al, Ga) as waveguide for low-density polariton condensation from a bound state in the continuum. *Phys. Rev. Appl.* **18**, 024039 (2022).
23. Hsu, C. W. et al. Bound states in the continuum. *Nat. Rev. Mater.* **1**, 16048 (2016).
24. Ha, S. T. et al. Directional lasing in resonant semiconductor nanoantenna arrays. *Nat. Nanotechnol.* **13**, 1042–1047 (2018).

25. Huang, C. et al. Ultrafast control of vortex microlasers. *Science* **367**, 1018–1021 (2020).
26. Hwang, M.-S. et al. Ultralow-threshold laser using super-bound states in the continuum. *Nat. Commun.* **12**, 4135 (2021).
27. Tian, J. et al. Optical Rashba effect in a light-emitting perovskite metasurface. *Adv. Mater.* **34**, 2109157 (2022).
28. Zhang, X. et al. Chiral emission from resonant metasurfaces. *Science* **377**, 1215–1218 (2022).
29. Rong, K. et al. Spin-valley Rashba monolayer laser. *Nat. Mater.* **22**, 1085–1093 (2023).
30. Zhen, B. et al. Topological nature of optical bound states in the continuum. *Phys. Rev. Lett.* **113**, 257401 (2014).
31. Murai, S. et al. Engineering bound states in the continuum at telecom wavelengths with non-bravais lattices. *Laser Photonics Rev.* **16**, 2100661 (2022).
32. Doeleman, H. M. et al. Experimental observation of a polarization vortex at an optical bound state in the continuum. *Nat. Photonics* **12**, 397–401 (2018).
33. Jin, J. et al. Topologically enabled ultrahigh-Q guided resonances robust to out-of-plane scattering. *Nature* **574**, 501–504 (2019).
34. Yin, X. et al. Observation of topologically enabled unidirectional guided resonances. *Nature* **580**, 467–471 (2020).
35. Wang, Y. et al. Highly controllable etchless perovskite microlasers based on bound states in the continuum. *ACS Nano* **15**, 7386–7391 (2021).
36. Maggiolini, E. et al. Strongly enhanced light-matter coupling of monolayer WS_2 from a bound state in the continuum. *Nat. Mater.* **22**, 964–969 (2023).
37. Tian, J. et al. Phase-change perovskite microlaser with tunable polarization vortex. *Adv. Mater.* **35**, 2207430 (2023).
38. Gianfrate, A. et al. Reconfigurable quantum fluid molecules of bound states in the continuum. *Nat. Phys.* **20**, 61–67 (2024).
39. Daskalakis, K. et al. Nonlinear interactions in an organic polariton condensate. *Nat. Mater.* **13**, 271–278 (2014).
40. Plumhof, J. D. et al. Room-temperature Bose-Einstein condensation of cavity exciton-polaritons in a polymer. *Nat. Mater.* **13**, 247–252 (2014).
41. Zhong, X. et al. Non-radiative energy transfer mediated by hybrid light-matter states. *Angew. Chem. Int. Ed.* **128**, 6310–6314 (2016).
42. Dusel, M. et al. Room temperature organic exciton-polariton condensate in a lattice. *Nat. Commun.* **11**, 2863 (2020).
43. Tang, J. et al. Room temperature exciton–polariton Bose-Einstein condensation in organic single-crystal microribbon cavities. *Nat. Commun.* **12**, 3265 (2021).
44. Berghuis, A. M. et al. Room temperature exciton-polariton condensation in silicon metasurfaces emerging from bound states in the continuum. *Nano Lett.* **23**, 5603–5609 (2023).
45. Berghuis, A. M. et al. Condensation of exciton–polaritons in a bound state in the continuum: effects of the excitation spot size and polariton transport. *ACS Nano* **18**, 31987–31994 (2024).
46. Samuel, I. D. W. & Turnbull, G. A. Organic semiconductor lasers. *Chem. Rev.* **107**, 1272–1295 (2007).
47. Kuehne, A. J. & Gather, M. C. Organic lasers: recent developments on materials, device geometries, and fabrication techniques. *Chem. Rev.* **116**, 12823–12864 (2016).
48. Dong, H. et al. Organic microcrystal vibronic lasers with full-spectrum tunable output beyond the Franck-Condon principle. *Angew. Chem. Int. Ed.* **130**, 3162–3166 (2018).
49. Wei, C. et al. Organic Janus microspheres: a general approach to all-color dual-wavelength microlasers. *J. Am. Chem. Soc.* **141**, 5116–5120 (2019).
50. Yoshida, K. et al. Electrically driven organic laser using integrated OLED pumping. *Nature* **621**, 746–752 (2023).
51. Wang, J. et al. Experimental observation of Berry phases in optical Möbius-strip microcavities. *Nat. Photonics* **17**, 120–125 (2023).
52. Liang, Q. et al. Circularly polarized lasing from a microcavity filled with achiral single-crystalline microribbons. *Angew. Chem. Int. Ed.* **135**, e202213229 (2023).
53. Dang, N. H. M. et al. Tailoring dispersion of room-temperature exciton-polaritons with perovskite-based subwavelength metasurfaces. *Nano Lett.* **20**, 2113–2119 (2020).
54. Su, R. et al. Observation of exciton polariton condensation in a perovskite lattice at room temperature. *Nat. Phys.* **16**, 301–306 (2020).
55. Houdré, R. et al. Nonlinear emission of semiconductor microcavities in the strong coupling regime. *Phys. Rev. Lett.* **85**, 2793 (2000).
56. Dang, N. H. M. et al. Realization of polaritonic topological charge at room temperature using polariton bound states in the continuum from perovskite metasurface. *Adv. Opt. Mater.* **10**, 2102386 (2022).
57. Peng, K. et al. Topological valley Hall polariton condensation. *Nat. Nanotechnol.* **19**, 1283–1289 (2024).
58. Zasedatelev, A. V. et al. A room-temperature organic polariton transistor. *Nat. Photonics* **13**, 378–383 (2019).
59. Coles, D. M. et al. Polariton-mediated energy transfer between organic dyes in a strongly coupled optical microcavity. *Nat. Mater.* **13**, 712–719 (2014).
60. Yagafarov, T. et al. Mechanisms of blueshifts in organic polariton condensates. *Commun. Phys.* **3**, 18 (2020).
61. Solli, D. & Hickmann, J. Study of the properties of 2D photonic crystal structures as a function of the air-filling fraction and refractive index contrast. *Opt. Mater.* **33**, 523–526 (2011).
62. Wu, S. et al. Manipulating luminescence of light emitters by photonic crystals. *Adv. Mater.* **30**, 1803362 (2018).
63. Chen, Y. et al. Compact spin-valley-locked perovskite emission. *Nat. Mater.* **22**, 1065–1070 (2023).
64. Wang, B. et al. Generating optical vortex beams by momentum-space polarization vortices centred at bound states in the continuum. *Nat. Photonics* **14**, 623–628 (2020).
65. Sun, W. et al. Lead halide perovskite vortex microlasers. *Nat. Commun.* **11**, 4862 (2020).
66. Kubo, S. et al. Tunable photonic band gap crystals based on a liquid crystal-infiltrated inverse opal structure. *J. Am. Chem. Soc.* **126**, 8314–8319 (2004).
67. Allemeier, D. et al. Emergence and control of photonic band structure in stacked OLED microcavities. *Nat. Commun.* **12**, 6111 (2021).

Acknowledgements

This work was supported financially by the National Natural Science Foundation of China (Grant Nos. 22090023 and 22375207), the Ministry of Science and Technology of China (Grant No. 2022YFA1204403), the Chinese Academy of Sciences (XDB0520203), and the New Cornerstone Science Foundation through the XPLORER PRIZE. M.T., L.M., and Y.V. acknowledge the financial support from the Würzburg-Dresden Cluster of Excellence on Complexity and Topology in Quantum Matter—ct.qmat (EXC 2147, project ID 390858490), and the German Research Foundation (MA 7968/2-1). Prof. Xinfeng Liu and Dr. Xin Zeng in National Center for Nanoscience and Technology are gratefully acknowledged for their help in the measurement of spatial and temporal coherence.

Author contributions

X.Y. and Y.S.Z. conceived the idea. H.D. and Y.S.Z. supervised the project. X.Y., Z.Z., and H.D. designed the experiments. X.Y. prepared the materials and conducted the optical measurements. M.T., L.M., and Y.V. performed the theoretical calculations and analysis. X.Y., M.T., J.Y., H.D., and Y.S.Z. analyzed the data and wrote the paper. All authors discussed the results and commented on the manuscript.

Competing interests

The authors declare no competing interests.

Additional information

Supplementary information The online version contains supplementary material available at https://doi.org/10.1038/s41467-025-57738-1.

Correspondence and requests for materials should be addressed to Libo Ma, Haiyun Dong or Yong Sheng Zhao.

Peer review information *Nature Communications* thanks the anonymous reviewers for their contribution to the peer review of this work. A peer review file is available.